

# Identification of cholesterol crystals in plaques of atherosclerotic mice using hyperspectral CARS imaging

Ryan S. Lim,<sup>1,\*†</sup> Jeffrey L. Suhlim,<sup>1,†,§,\*\*\*</sup> Shinobu Miyazaki-Anzai,<sup>§§</sup> Makoto Miyazaki,<sup>§§</sup> Moshe Levi,<sup>§§</sup> Eric O. Potma,<sup>†,\*\*\*,††</sup> and Bruce J. Tromberg<sup>2,†,§,\*\*\*</sup>

Department of Physiology and Biophysics,\* Laser Microbeam and Medical Program (LAMMP),<sup>†</sup> Beckman Laser Institute, Department of Biomedical Engineering,<sup>§</sup> Center for Complex Biological Systems,\*\* and Department of Chemistry,<sup>††</sup> University of California, Irvine, CA; and Division of Renal Diseases and Hypertension,<sup>§§</sup> Department of Medicine, University of Colorado, Denver, CO

**Abstract** The accumulation of lipids, including cholesterol, in the arterial wall plays a key role in the pathogenesis of atherosclerosis. Although several advances have been made in the detection and imaging of these lipid structures in plaque lesions, their morphology and composition have yet to be fully elucidated, particularly in different animal models of disease. To address this issue, we analyzed lipid morphology and composition in the atherosclerotic plaques of two animal models of disease, the low density lipoprotein receptor-deficient (LDLR<sup>-/-</sup>) mouse and the ApoE lipoprotein-deficient (ApoE<sup>-/-</sup>) mouse, utilizing hyperspectral coherent anti-Stokes Raman scattering (CARS) microscopy in combination with principal component analysis (PCA). Hyperspectral CARS imaging revealed lipid-rich macrophage cells and condensed needle-shaped and plate-shaped lipid crystal structures in both mice. Spectral analysis with PCA and comparison to spectra of pure cholesterol and cholesterol ester derivatives further revealed these lipid structures to be pure cholesterol crystals, which were predominantly observed in the ApoE<sup>-/-</sup> mouse model. These results illustrate the ability of hyperspectral CARS imaging in combination with multivariate analysis to characterize atherosclerotic lipid morphology and composition with chemical specificity, and consequently, provide new insight into the formation of cholesterol crystal structures in atherosclerotic plaque lesions.—Lim, R. S., J. L. Suhlim, S. Miyazaki-Anzai, M. Miyazaki, M. Levi, E. O. Potma, and B. J. Tromberg. Identification of cholesterol crystals in plaques of atherosclerotic mice using hyperspectral CARS imaging. *J. Lipid Res.* 2011. 52: 2177–2186.

**Supplementary key words** atherosclerosis • LDL receptor • ApoE • hyperspectral coherent anti-Stokes Raman scattering • nonlinear optical microscopy • principal component analysis

This work was supported by National Institutes of Health Grants U01-DK-076134, R01-AG-026529, R01-DK-066029, and P41-RR-01192 (Laser Microbeam and Medical Program, LAMMP); by American Heart Association Grant 10BGIA4580053; by the Beckman Foundation; and by Center for Complex Biological Systems (CCBS) Grant P50-GM-076516. Its contents are solely the responsibility of the authors and do not necessarily represent the official views of the National Institutes of Health or other granting agencies.

Manuscript received 20 June 2011 and in revised form 22 September 2011.

Published, JLR Papers in Press, September 23, 2011  
DOI 10.1194/jlr.M018077

The accumulation of lipids within the arterial wall plays a critical role in the progression of atherosclerosis. As monocytes are recruited to the vessel wall during the initial inflammatory response, they differentiate into macrophage cells and begin to ingest oxidized low density lipoproteins (LDL), thus forming specialized foam cells (1–3). The LDL particles, which are rich in cholesterol, are unable to be processed by the macrophages and therefore cause the foam cells to eventually rupture. The death of these foam cells further propagates the inflammatory process, recruiting more monocyte-derived macrophages and consequently leaving behind a growing pool of cholesterol and other lipophilic compounds (4–6). Cholesterol, in the form of cholesterol crystals (ChC), plays a particularly prominent role in the atherogenic process and serves as a marker for advanced atherosclerotic lesions (7–9). Studies have shown that these crystals exist within sites of plaque rupture, but they are typically absent from deceased patients who suffered from severe atherosclerosis (but not as their primary cause of death), thereby suggesting an important link between ChC formation and atherosclerosis-related death (6, 10, 11). Recently, ChCs have been recognized as capable of inducing an inflammatory response through stimulation of the caspase-1-activating NLRP3 inflammasome (8, 9). In addition, the formation of extracellular ChC material has been implicated as a mechanical factor that contributes directly to plaque vulnerability (10, 12).

As such an essential component of the atherosclerotic process, lipids have been the target of several recent imaging studies. These studies have utilized both noninvasive and invasive modalities to image lipid-rich regions and characterize general plaque morphology. Noninvasive

Abbreviations: CARS, coherent anti-Stokes Raman scattering; CH, carbon-hydrogen bond; ChC, cholesterol crystal; LDLR, low density lipoprotein receptor; PCA, principal component analysis.

<sup>1</sup>R. S. Lim and J. L. Suhlim contributed equally to this work.

<sup>2</sup>To whom correspondence should be addressed.  
e-mail: bjtrombe@uci.edu

methods, such as computed tomography (CT) and magnetic resonance imaging (MRI), provide general information about plaque structure, such as the degree of stenosis and the presence of lipid-rich tissue, respectively (13–15). These methods, although informative of general plaque morphology and features of the vessel wall, typically suffer from either poor contrast resolution (CT) or poor spatial resolution (MRI), and therefore preclude analysis at the cellular level. Invasive techniques, however, such as intravascular ultrasound (IVUS) and optical coherence tomography (OCT), have shown potential for yielding structural and chemical information at a highly detailed level (16–18). These methods are currently under investigation in large-scale clinical trials. Although these modalities provide insight into plaque structure, they typically require the use of exogenous dyes to provide contrast in the tissue. Furthermore, none of these existing imaging techniques permits chemically selective detection of ChCs. These limitations necessitate the need for label-free, high-resolution imaging techniques that can simultaneously provide rich, spatially resolved chemical information.

Nonlinear optical microscopy provides a label-free means for imaging key components in biological tissue at submicron resolution and with highly specific chemical identification (19–21). One nonlinear technique - coherent anti-Stokes Raman scattering (CARS) - has emerged as an ideal method for selective imaging of lipids (21–23). By probing the intrinsic vibrational signatures of carbon-hydrogen (CH) bonds, CARS microscopy can easily detect CH-rich lipid structures in tissue. Consequently, CARS, in addition to other nonlinear microscopy techniques, has been applied to several studies on atherosclerosis, including the visualization of extracellular lipids and lipid-rich cells associated with plaque lesions (24, 25) and the determination of lipid concentration levels in various lesions of the arterial intima (26, 27). Previous work of our own utilized a multimodal CARS-based imaging technique to determine the impact of diet on macrophage infiltration and lipid accumulation in early-stage atherosclerotic plaques (28).

Although these studies demonstrate the ability of CARS to detect lipids in atherosclerotic tissue, determining the exact composition of these lipid structures remains a difficult, yet important, endeavor. In fact, studies have shown that the composition of the plaque, rather than its size, determines plaque stability (29). Recently, Kim et al. used a multiplex CARS imaging system to identify four general morphologies of atherosclerotic lipids and characterize their chemical profiles (30). They were able to acquire CARS spectra in the 2,650–3,050  $\text{cm}^{-1}$  range from regions with distinct lipid morphology, and it was concluded that changes in the spectra were due to modifications of the lipids during the course of disease progression. Nonetheless, the exact makeups of the lipid structures and pools, which include cholesterol and cholesteryl esters, have yet to be fully determined. Furthermore, spectral acquisition using multiplex CARS, although undoubtedly faster than conventional Raman

spectroscopy, is typically implemented only at selected pixels of interest. As compositional variation within the tissue cannot be assumed to simply be a function of morphology (i.e., spectra acquired from selected pixels do not necessarily reflect the composition of the overall structure), spatially resolved molecular maps are required to better connect lipid composition and distribution to plaque progression.

In this work, we aim not only to identify atherosclerotic lipid structures in plaque lesions but also to address their composition. Specifically, we aim to track the distribution of molecular compounds that have been shown to play major roles in atherogenesis, particularly cholesterol and its derivatives. To selectively detect these compounds in plaque lesions, we have advanced the CARS imaging method such that spectrally resolved molecular maps of the lesion can be taken. Supplementing coherent Raman images with spectral information enables the visualization of several lipid classes selectively (31). Our method is based on hyperspectral CARS imaging, which was recently successfully used to unveil the compositional lipid variations in gland tissues (32). Here we use hyperspectral CARS in combination with principal component analysis (PCA) to extract spectrally significant variations of molecular distributions throughout the lesion. PCA is a statistical analysis tool that enables multidimensional datasets (i.e., hundreds of thousands of pixels taken at multiple wavelengths) to be reexpressed in terms of fewer variables (33). In this study, we demonstrate that, with PCA, major constituents can be discriminated based on the correlated spectral variations within the dataset itself, thereby providing an unsupervised and efficient assessment of chemical composition. On this note, the application of PCA for dimensionality reduction, in lieu of other nonlinear techniques, has been recently highlighted (34), and its utility for spectral decomposition and image reconstruction of hyperspectral CARS datasets has been illustrated in several studies (35, 36), including our own work (32).

The combined hyperspectral CARS imaging/PCA method has allowed us to examine lipid structures in plaque lesions with greatly improved chemical detail. Importantly, we have found that this technique can successfully discriminate lipophilic compounds, in both intra- and extracellular regions, in a label-free manner. We have applied this method to study the structure and chemical makeup of plaques in two atherosclerotic mouse models: the LDL receptor-deficient ( $\text{LDLR}^{-/-}$ ) mouse and the ApoE-deficient ( $\text{ApoE}^{-/-}$ ) mouse (37–41). Our label-free imaging results reveal clusters of macrophage cells as well as needle-shaped and plate-shaped lipid crystal structures within plaque lesions. Our CARS spectral analysis further establishes that a large fraction of these condensed crystal microstructures are, in fact, ChCs. These results provide important information about plaque morphology and composition, and consequently, carry strong implications on the structural development and progression of plaques during atherogenesis.

### Atherosclerotic mouse models and sample handling

The 5/6 nephrectomized ApoE-deficient (ApoE<sup>-/-</sup>; stock #002052, n = 6) and LDL receptor-deficient (LDLR<sup>-/-</sup>; stock #002207, n = 6) mice were purchased from Jackson Laboratory (Bar Harbor, ME). Details of 5/6 nephrectomy were previously described (42). Mice were first anesthetized with ketamine/Xylazine. The left kidney was then decapsulated and one-third of each kidney pole ligated with a silk suture. The kidney tissue from each pole was excised with scissors. The muscle and skin layers of the incision were then closed with sterile surgical staples. The animals recovered for one week before undergoing a second surgery, in which the entire right kidney was decapsulated and surgically removed by ligating with a silk suture at the bottom of the renal artery and then excising the tissue with scissors. At 8 weeks of age, animals were fed a Western diet containing 0.15% cholesterol and 21% milk fat (TD88137, Harlan Teklad, Indianapolis, IN) for 16 weeks. Animals were euthanized and then perfused with 4% buffered paraformaldehyde. Serum cholesterol and triglyceride levels were determined by enzymatic methods (Thermo Fisher Scientific, Waltham, MA).

For microscopic examination, complete aortas were removed, opened longitudinally from the heart to the iliac arteries, and mounted on a glass coverslip, luminal side faced down for en face imaging on the inverted microscope. Phosphate buffered saline (PBS) solution was added to prevent the tissue from drying out, and a second coverslip was secured with nail polish on top of the artery to prevent motional artifacts. Animal experiments were approved by the Institutional Animal Care and Research Advisory Committee of the University of Colorado at Denver.

### Cholesterol, cholesteryl esters, and triglyceride

Pure cholesterol, tristearin (a triglyceride), and three cholesteryl ester forms (palmitate, oleate, and linoleate) were purchased from Sigma-Aldrich and used without further purification. Tristearin and the cholesteryl esters were solubilized in chloroform and allowed to recrystallize on glass coverslips for CARS spectroscopic examination. Cholesterol monohydrate crystals were grown by recrystallizing cholesterol in water. Bovine serum albumin (BSA) was obtained from Sigma-Aldrich. A saturated aqueous solution of BSA was placed adjacent to the crystal of the lipophilic compound on the coverslip to provide a generic protein reference spectrum within the same field of view (43).

### CARS imaging and spectral analysis

The pump and Stokes beams required for the CARS process were derived from an optical parametric oscillator (Levante Emerald OPO, Berlin, Germany) pumped by a 76 MHz mode-locked Nd:vanadate laser (Picotrain, High-Q, Hohenems, Austria). The fundamental 1,064 nm, 7 ps pulses of the Nd:vanadate laser source provided the Stokes radiation, while the second harmonic 532 nm light was used to pump the OPO (generating tunable wavelength from 780–830 nm). The collinearly overlapped pump and Stokes beams were passed through a laser scanner (Fluoview 300, Olympus, Center Valley, PA) and focused with a 20 $\times$ , 0.75 NA objective lens (UplanS Apo, Olympus) onto the sample. Images were collected for vibrational frequencies in the range 2,760–3,060 cm<sup>-1</sup> in intervals of approximately 4 cm<sup>-1</sup> for 64 different wavelengths (Fig. 1). This vibrational region has been previously identified to contain the most spectral variation for various cholesterol subclasses (44). The range of vibrational frequencies was achieved by spectral tuning of the OPO, which has been recently discussed in detail (45). Average acquisition time for one hyperspectral data stack was 20 min.

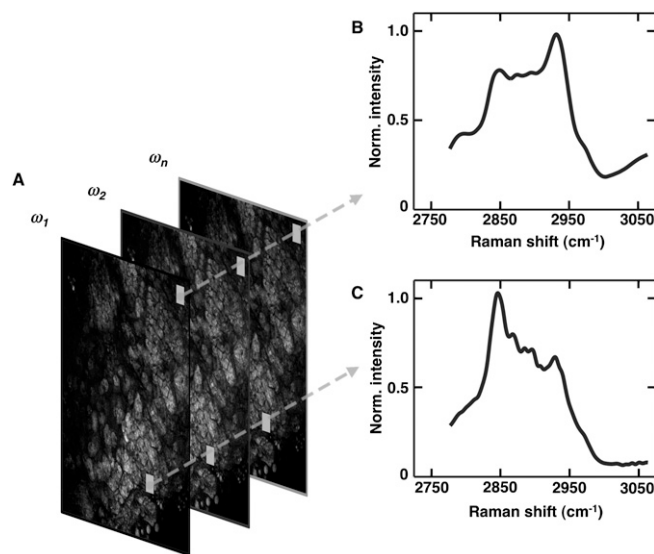


**Fig. 1.** Principle of hyperspectral CARS imaging. A: High-resolution spectral maps were obtained by rapidly scanning the frequency difference between the pump and Stokes pulse pair during consecutive image acquisition. The X by Y area ( $\mu\text{m}^2$ ) is scanned at consecutive wavenumbers ( $\omega_n$ ), forming a 3D data stack ( $x, y, n$ ). Each pixel in the XY plane now contains a vibrational spectrum. Shown here are CARS images obtained from the aortic arch of an ApoE<sup>-/-</sup> mouse. B: Typical CARS protein spectrum. C: Typical CARS lipid spectrum.

### Principal component analysis

PCA is a chemometric method that reduces the dimensionality of the data, based on the variance in the data itself, into a new coordinate system, also known as principal components (33). In this study, we utilized PCA to decompose the hyperspectral data in terms of a manageable set of principal components that best describes the spectral variations in the original data. Detailed descriptions on the implementation of PCA for image analysis can be found in several reviews (46, 47), and its applications for hyperspectral CARS imaging has been recently demonstrated (32, 36).

Briefly, the hyperspectral data ( $x, y, \omega$ ) can be organized in a single matrix  $Y$ , where each column corresponds to intensities measured at different vibrational frequencies. Hence, for a 512-by-512 image,  $Y$  typically consists of 262,144 rows and 64 columns, corresponding to the total number of pixels and total number of spectral points, respectively. In some cases, several datasets are combined to statistically improve the classification of major components in the image. MATLAB's Singular Value Decomposition (SVD) function was used to compute eigenvectors ( $V$ ) and eigenvalues ( $D$ ). Subsequently, the principal components matrix ( $Z$ ) is calculated based on  $Z = YV$ , exclusively incorporating eigenvectors that contain the most significant variance. Prior to decomposition,  $Y$  is centered by subtracting the mean intensity for each column from each pixel.

In addition to dimensionality reduction, the spectra from each pixel can also be generated by using selected principal components ( $p$ ), thereby minimizing the unwanted contribution from noise in the data. For this purpose, the eigenvectors in matrix  $V$  are arranged in a decreasing fashion based on the magnitude of its corresponding eigenvalues. The spectra ( $S$ ) are then computed as  $S = Z_p V_p^T$ , where  $Z_p$  and  $V_p$  are the truncated principal components and eigenvectors, respectively. For most datasets, the first three principal components account for more than 80% of the variances. In our previous work, we showed that the

reconstructed spectra based on the selected principal components,  $S$ , are identical to the original CARS spectra, thus confirming that the linear transformation and subsequent spectral reconstruction in PCA do not distort the intrinsic features contained in the raw dataset. Because of the undistorted reproduction of the original CARS spectra, the spectral comparison can be performed directly on the CARS dataset without the need for converting the data to linear Raman spectra with phase retrieval algorithms (32). To enhance the contrast among different constituents in the image, the RGB scoremap is generated based on new axes,  $Z_p$ , where the spectra from the same colored pixels are averaged and normalized to the peak value. To further facilitate visualization, structures of interest are colored green, red, yellow, violet, and orange, with other compounds colored blue.

### Quantitative analysis

Lipid-rich crystal structures, specifically needle-shaped and plate-shaped crystals, were quantitatively analyzed in both ApoE<sup>-/-</sup> and LDLR<sup>-/-</sup> mice. Specifically, the gross accumulation of cholesterol-associated needle and plate structures was calculated as a function of total tissue area (i.e., number of crystal structures per 125,000  $\mu\text{m}^2$ ). To calculate the number of cholesterol crystal structures, only the fraction of each individual image with spectra similar to pure cholesterol monohydrate (obtained from the PCA-derived scoremaps and then compared with the pure lipid components) was considered in our analysis. Images were then cross-referenced with their original CARS images to match spectral features with morphologic features, thus allowing for an accurate assessment of only cholesterol-associated crystal structures. CARS images from all wavelengths within our range of vibrational frequencies (2,760–3,060  $\text{cm}^{-1}$ ) were analyzed to ensure an accurate spatial assessment of all crystals. All values were compared using the  $t$  test. All  $P$  values less than 0.05 were considered statistically significant.

### Lipid-rich macrophage cells

CARS images of lipid-rich structures within the aortic walls of LDLR<sup>-/-</sup> mice are shown in Fig. 2. These structures, which are defined by rounded morphologies and distinct dark nuclei, are identified as clusters of macrophage cells (28). Images were acquired at various regions of the aorta, including the descending/thoracic aorta (Fig. 2A), the ascending aorta (Fig. 2B), and the abdominal aorta (Fig. 2C), thus indicating a broad distribution of macrophage cells throughout the entire artery.

A scoremap (Fig. 2D) and corresponding CARS spectra (Fig. 2E) derived from the PCA of a representative macrophage CARS image (Fig. 2A) were also generated. Two major contributing CARS spectra are seen. The first type of spectra (green spectrum) reveals a typical lipid profile characterized by the strong peak of the CH<sub>2</sub> symmetric vibration at 2,845  $\text{cm}^{-1}$ . Lipid spectra of similar profile have previously been associated with pools of neutral lipids, such as long-chain aliphatic triglycerides (23). This type of spectra is prevalent in all regions of the image that can be associated with macrophages. The second type of spectra (red spectrum) yields major peaks at 2,845  $\text{cm}^{-1}$ , 2,865  $\text{cm}^{-1}$ , 2,905  $\text{cm}^{-1}$ , 2,945  $\text{cm}^{-1}$ , and 2,965  $\text{cm}^{-1}$ . This spectral signature, although markedly different from the first type of spectra, also appears to associate with some of the macrophage cells in the image, therefore suggesting either compositional variation within the macrophage population or the presence of other, spectrally unique lipid structures within the macrophage cells.

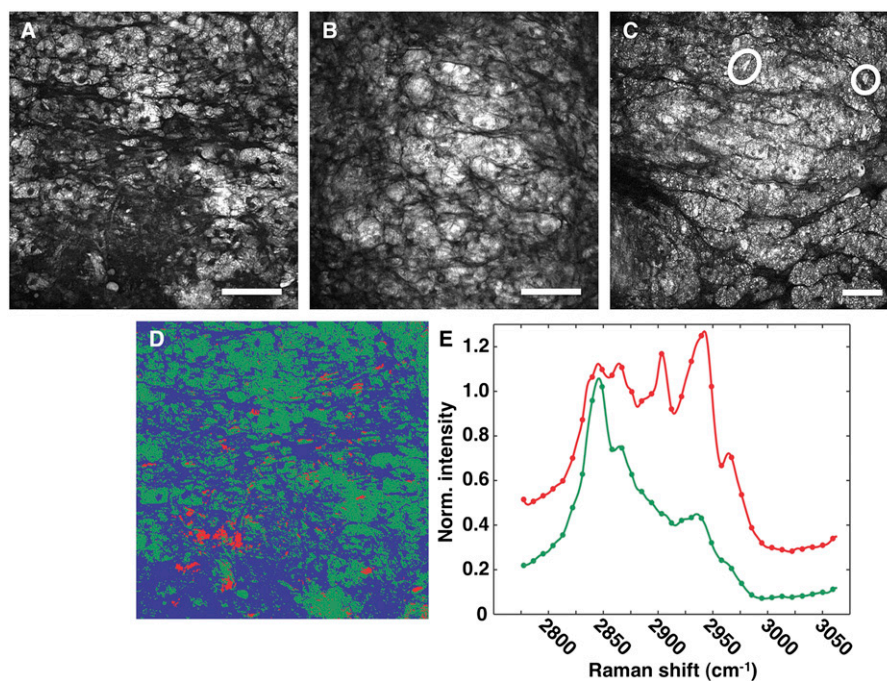


**Fig. 2.** CARS images of lipid-rich macrophage cells in LDLR<sup>-/-</sup> mice and corresponding PCA. Images were obtained from the descending aorta (A), the ascending aorta (B), and the lower abdominal aorta (C). Some thin, needle-shaped structures, indicated by circles in (C), were observed. A scoremap (D) was derived from the PCA of the CARS image in (A). CARS spectra (E) from the green and red regions of the scoremap were reconstructed, with the spectra offset for clarity. Scale bar: 50  $\mu\text{m}$ .

CARS images of lipid-rich structures in the ApoE<sup>-/-</sup> mice are shown in Fig. 3. Similar to the LDLR<sup>-/-</sup> mice, dense macrophage cell clusters are seen in lesions throughout the entire length of the aorta (Fig. 3A–C). A corresponding scoremap (Fig. 3D) and CARS spectra derived from PCA (Fig. 3E) were also generated. A significant fraction of the macrophage cells exhibit intracellular lipids that spectrally resemble the lipids contained in the macrophage cells of the LDLR<sup>-/-</sup> mouse, as characterized by the lipid-like spectrum in Fig. 3E (green spectrum). We also find additional spectral signatures among the intracellular lipids in the ApoE<sup>-/-</sup> model. As shown in Fig. 3D, some cells exhibit a distinct spectrum that features a prominent peak at 2,930 cm<sup>-1</sup> (orange spectrum). This spectrum, which was also evident in some regions of the LDLR<sup>-/-</sup> mouse (data not shown), corresponds to a composition of lipophilic compounds that is different from the typical long-chain aliphatic lipid spectrum. Some cells in the image show both types of spectra in distinct intracellular domains. It can be seen that, within the sensitivity of the experiment, the CARS spectrum in the macrophage cells is heterogeneous.

#### Needle-shaped and plate-shaped lipid crystals

In addition to macrophage cells, other well-defined lipid structures are evident in both LDLR<sup>-/-</sup> and ApoE<sup>-/-</sup> mouse models. In particular, as shown in Fig. 4, we observe thin, needle-like structures (“needles”) and flat, rectangular plate-shaped structures (“plates”) in the ApoE<sup>-/-</sup> lesions. Similar structures were previously observed

by Kim et al. (30). These needles and plates appear to form at various locations along the artery, with some located in close proximity to other lipid-rich structures (Fig. 4A, D) and others in more isolated regions (Fig. 4E). Fig. 4C and F show electronically zoomed-in (8×) views of the needles and plates, respectively. These zoomed-in images, specifically Fig. 4F, reveal even further the complex nature of these lipid-based structures (e.g., smaller plates within the larger plate).

In Fig. 5, a CARS image of representative needles (Fig. 5A), its PCA-derived scoremap (Fig. 5B), and its corresponding CARS spectra (Fig. 5C) are shown. In Fig. 5B, the needle structures are characterized by several distinct spectra (green and red). This suggests that there exists compositional variation even within structures of apparent morphologic similarity. Neighboring lipid-rich cell clusters vary in compositional makeup as well, as some share the same composition as the needles (the green and red regions), whereas others maintain a slightly different constituency (yellow regions). The corresponding CARS spectra in Fig. 5C support these findings. The green spectrum assigned to some of the needle structures and cell clusters exhibits a strong major peak at the lipid CH<sub>2</sub> symmetric stretching vibration (~2,845 cm<sup>-1</sup>). However, the red and yellow spectra assigned to other needles and cell clusters exhibit additional strong peaks at 2,845 cm<sup>-1</sup>, 2,865 cm<sup>-1</sup>, 2,905 cm<sup>-1</sup>, 2,945 cm<sup>-1</sup>, and 2,965 cm<sup>-1</sup>, in agreement with the CARS point-spectra previously taken at selected crystals (30). This second spectral signature is also similar to the secondary type of spectra observed in some of the

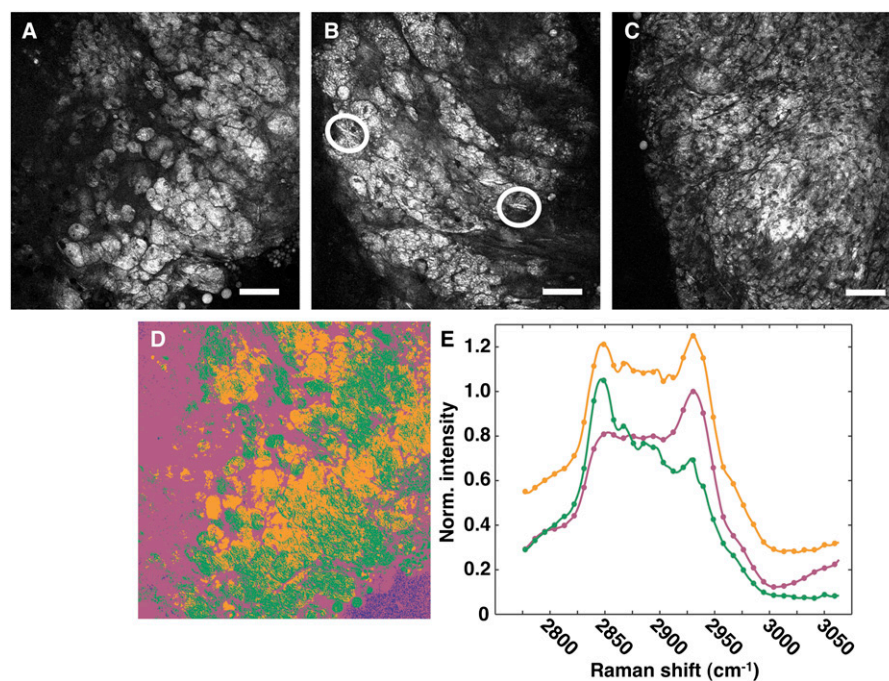


**Fig. 3.** CARS images of lipid-rich macrophage cells in ApoE<sup>-/-</sup> mice and corresponding PCA. Images were obtained from the aortic arch (A) and the ascending aorta (B, C). Some thin, needle-shaped structures, indicated by circles in (B), were observed. A scoremap (D) was derived from the PCA of the CARS image in (A). CARS spectra (E) from the green, purple, and orange regions of the scoremap were reconstructed, with the spectra offset for clarity. Scale bar: 50 μm.

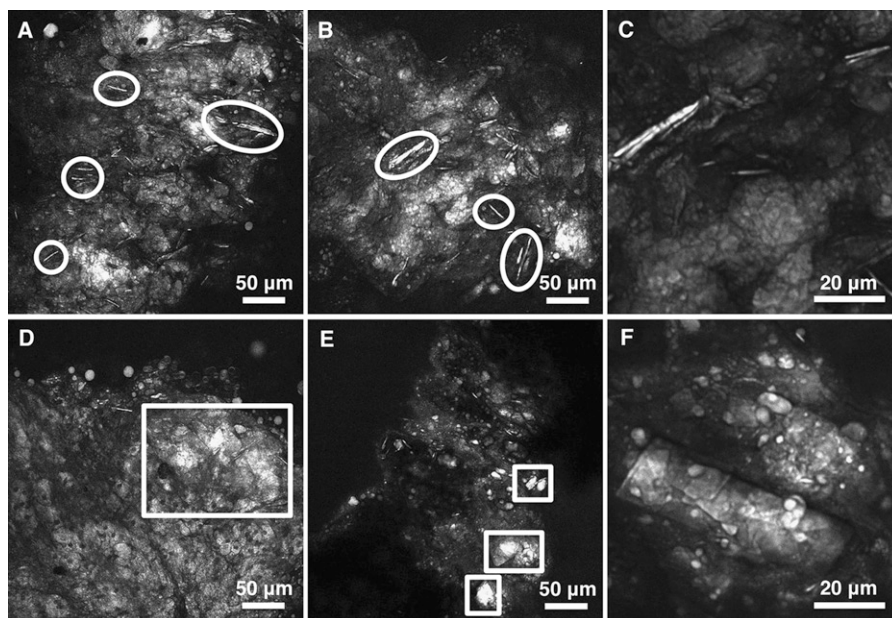


**Fig. 4.** CARS images of various lipid-rich structures in ApoE<sup>-/-</sup> mice. Thin, needle-shaped structures, some indicated by circles in (A–B), and flat, rectangular plate-shaped structures, some indicated by boxes in D–E, were observed. Electronically zoomed-in (8×) images were also obtained (C, F) to highlight the needle and plate structures, respectively.

macrophage cells of the LDLR<sup>-/-</sup> mouse (Fig. 2E, red spectrum). This further supports the theory that other spectrally unique lipid structures (in this case, needles) may reside within the macrophage cells.

**Fig. 6** provides a hyperspectral CARS analysis of the observed plate-like structures. The red and yellow regions associated with the plate structure in Fig. 6B yield spectra that are similar to the red and yellow regions of the needles, but they are different from the predominantly green spectrum of the surrounding lipid-rich regions (only one dominant peak at  $\sim 2,845$  cm<sup>-1</sup>). Similar to the needle structures, plates with similar morphology also contain spectral variation. These spectral variations implicate the existence of compositional variations within the different lipid-based structures. This finding contrasts a prior study that correlated specific morphologic features with composition (30).

#### Cholesterol, cholesteryl esters, and triglyceride

To facilitate a direct comparison between the spectral profiles of the LDLR<sup>-/-</sup> and ApoE<sup>-/-</sup> lipid crystal structures and the spectral profiles of known plaque components, hyperspectral CARS imaging of pure cholesterol monohydrate, triglyceride (tristearin), and three forms of cholesteryl esters (cholesteryl palmitate, oleate, and linoleate) was carried out. These cholesteryl esters were chosen because they form main contributions to the LDL lipid content (48). BSA was analyzed as a control with a known protein spectrum. The results are shown in **Fig. 7**. The CARS spectrum of pure cholesterol monohydrate exhibits strong characteristic peaks at 2,905 cm<sup>-1</sup> and 2,945 cm<sup>-1</sup>. Cholesteryl linoleate yields a similar spectral profile but without the 2,945 cm<sup>-1</sup> (instead, slightly shifted to 2,930 cm<sup>-1</sup>) and 2,965 cm<sup>-1</sup> peaks. Cholesteryl oleate displays a much more pronounced contribution from the

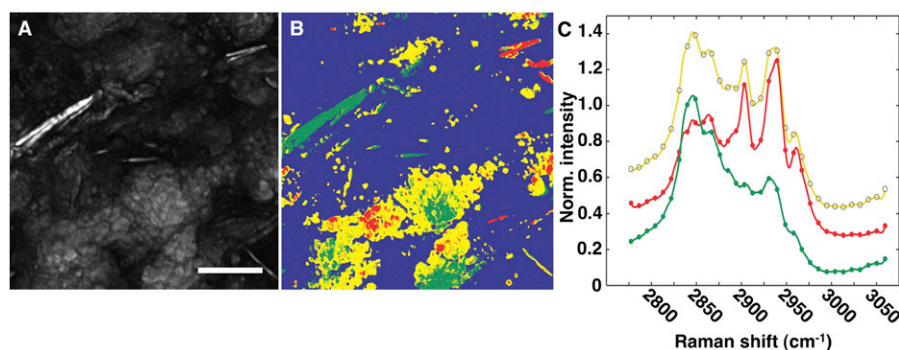


**Fig. 5.** PCA of needle-shaped lipid structures in ApoE<sup>-/-</sup> mice. A scoremap (B) was derived from PCA of the CARS image (A). CARS spectra (C) from the green, red, and yellow regions of the scoremap were reconstructed, with the spectra offset for clarity. Scale bar: 20 μm.

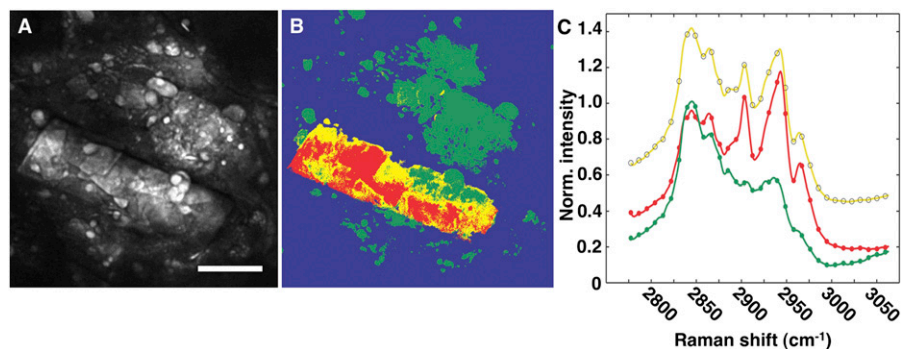


**Fig. 6.** PCA of plate-shaped lipid structures in ApoE<sup>-/-</sup> mice. A scoremap (B) was derived from PCA of the CARS image (A). CARS spectra (C) from the green, red, and yellow regions of the scoremap were reconstructed, with the spectra offset for clarity. Scale bar: 20  $\mu\text{m}$ .

symmetric CH<sub>2</sub> vibration at 2,845 cm<sup>-1</sup>. Tristearin and cholesteryl palmitate both yield strong CARS peaks at  $\sim 2,845$  cm<sup>-1</sup> and  $\sim 2,885$  cm<sup>-1</sup>, whereas the protein reference (BSA) shows a distinct, typical protein profile with a maximum at  $\sim 2,930$  cm<sup>-1</sup>.

### Quantitative analysis of lipid-rich crystal structures

From the hyperspectral CARS analysis of the needle-shaped and plate-shaped crystal structures illustrated in Figs. 5 and 6, we observe two predominant spectral signatures (red and yellow spectra) that directly correspond to pure cholesterol monohydrate, as evident by the hyperspectral analysis of pure cholesterol and cholesteryl esters (Fig. 7, further elaborated in the “Discussion” section). To quantitatively determine the amount of cholesterol-rich crystals in both ApoE<sup>-/-</sup> and LDLR<sup>-/-</sup> mice, only the fraction of each individual image (from the PCA-derived scoremaps in Figs. 5B and 6B) with spectra similar to pure cholesterol monohydrate was considered in our analysis. These images were then cross-referenced with their original CARS images to match spectral features with morphologic features, thus allowing for an accurate assessment of only cholesterol-associated crystal structures. The total number of crystals was calculated as a function of total tissue area (i.e., number of crystal structures per 125,000  $\mu\text{m}^2$ ), thereby revealing the abundance of cholesterol-associated crystal structures within each transgenic model. Fig. 8 reveals a significant increase in cholesterol-associated crystal structures within the lesions of the ApoE<sup>-/-</sup> mice versus the LDLR<sup>-/-</sup> mice ( $8.8421 \pm 2.2881$  versus  $3.0167 \pm 0.7581$ ,  $P = 0.0183$ ).

## DISCUSSION

We have demonstrated that morphologic and compositional features of lipid-rich atherosclerotic plaques can be determined in two murine models of disease: the LDLR<sup>-/-</sup> mouse and the ApoE<sup>-/-</sup> mouse. Utilizing hyperspectral CARS imaging in combination with multivariate analysis, we specifically observed large, broad clusters of lipid-rich macrophage cells, as well as thin, needle-shaped lipid structures and flat, rectangular-shaped lipid plates, within aortic plaques. We further determined the composition of

these crystalline structures and identified them as pure cholesterol crystals. Quantitative analysis also revealed that these cholesterol-rich crystal structures were significantly more abundant in the ApoE<sup>-/-</sup> mouse compared with the LDLR<sup>-/-</sup> mouse, thus suggesting the possibility of different mechanisms of plaque development between the two disease models. Our findings exemplify the ability of hyperspectral CARS with principal component analysis to precisely detect physical and compositional changes within the atherosclerotic plaques.

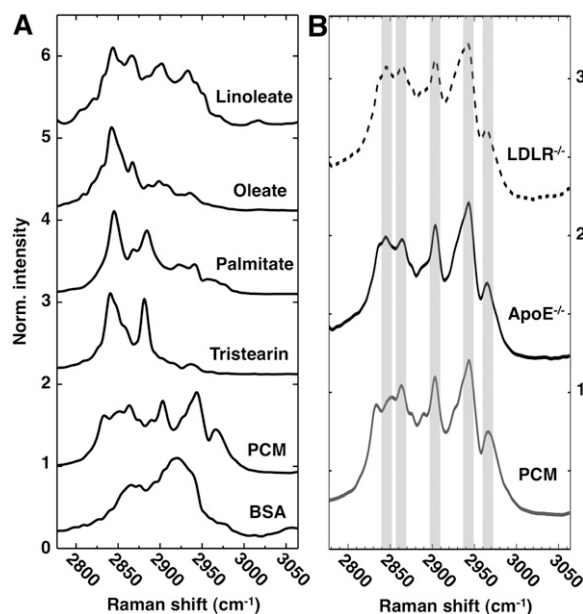


**Fig. 7.** CARS spectra of known lipid-rich plaque components and comparison to acquired spectra. Pure cholesterol monohydrate (PCM), tristearin, cholesteryl palmitate, cholesteryl oleate, and cholesteryl linoleate were analyzed (A). CARS spectrum of BSA was included as a control. The two dominant spectra obtained from the lipid structures of both ApoE<sup>-/-</sup> and LDLR<sup>-/-</sup> mice (dashed line and solid black line) were compared with the pure cholesterol monohydrate spectrum (solid gray line), with corresponding peaks highlighted (shaded regions, B). Each CARS spectrum was shifted vertically for direct comparison.

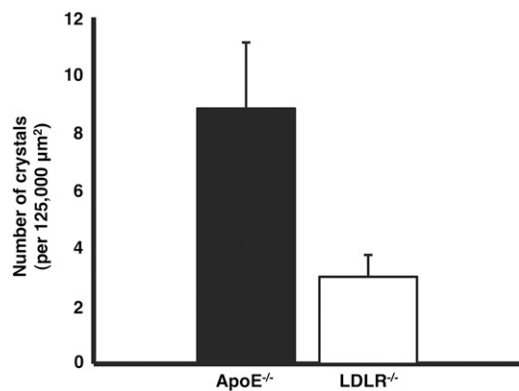


**Fig. 8.** Quantitative analysis of cholesterol-associated crystal structures in ApoE<sup>-/-</sup> (black) and LDLR<sup>-/-</sup> (white) mice. The total number of crystal structures was determined by considering only the fraction of each individual image (seen in the PCA score-maps) with spectra similar to the pure cholesterol monohydrate spectrum, and then cross-referencing with the individual CARS images to match spectral features with morphologic features. Total tissue area per image was 125,000 μm<sup>2</sup>.  $P < 0.05$ .

### CARS spectral analysis of lipophilic components

In this study, we have used CARS hyperspectral imaging to gain insight into the distribution and composition of intra- and extracellular lipid-rich pools in plaque lesions. We have limited ourselves to the spectral region of the CH stretching vibrations. This region is known to produce very strong CARS signals, while maintaining a high degree of spectral differentiation among major classes of lipophilic compounds. The CARS signal is related to the Raman spectrum of the molecular compounds in focus, although the features in CARS spectra are generally broader and the amplitude of the higher energy band vibrations is generally lower due to interferences with the nonresonant background. In principle, the CARS spectra can be converted to Raman spectra with the aid of phase retrieval algorithms. To avoid conversion artifacts due to the spectral range examined, we have chosen to analyze the vibrational information contained in the CARS spectra by direct comparison with the CARS spectra in situ of the major lipophilic compounds found in plaque lesions. Such a comparison is warranted in the case of pure states of the compound, as is the case for crystalline materials. Furthermore, PCA is performed to facilitate spectral discrimination, and its unsupervised nature allows for efficient and direct analysis without knowledge of the sample composition. We note that the principal components are assembled strictly based on linear combinations of mutually correlated variables in the dataset itself. It has been previously shown that spectral reconstructions using the principal components do not distort the intrinsic spectral features contained in the raw dataset (32).

The CARS spectral analysis reveals four major spectral classes in the plaques. The CARS spectrum of the first class resembles the spectral signatures of long-chain fatty acids and triglycerides in the fluid or crystalline fluid phase, with a strong major peak at 2,845 cm<sup>-1</sup>. This lipid-rich pool is predominantly found in macrophages that have infiltrated the lesions, which are evident in both the

LDLR<sup>-/-</sup> and ApoE<sup>-/-</sup> models. This lipid type is also found in needle- and plate-like microsols. The second class is characterized by a similar CARS spectrum but with a more prominent peak at 2,930 cm<sup>-1</sup>, which is also found within the macrophage population. The compositional origin of this spectrum is unclear, but it is likely a mixture of lipophilic compounds and protein-rich structures. The third class constitutes condensed needle- and plate-like lipid structures characterized by two strong peaks at 2,905 and 2,945 cm<sup>-1</sup>. These needles and plates exhibit rectangular shapes and are thus crystalline in nature. For these crystalline materials, a direct comparison with the in situ spectra in Fig. 7 is possible. Within experimental uncertainty, the spectrum associated with these crystal structures is identical to the cholesterol monohydrate spectrum. Therefore, we attribute this spectral class to the presence of ChCs in the tissue. Finally, the last class is formed by the protein-like spectrum of the extracellular matrix, which, as expected, is retrieved in both mouse models.

Given the important role of ChCs in atherogenesis, the ability to detect ChCs with chemical selectivity in unstained arterial tissue is significant. Previous optical microscopy studies have utilized confocal reflection microscopy to identify ChCs in macrophage cells in tissue cultures and in prepared arterial tissue slices (8, 9). Whereas reflection microscopy is sensitive to the enhanced reflectivity of ChCs, it is not chemically selective and thus cannot discriminate between ChCs and other condensed materials in the plaque. In our study, for instance, we have found that the microscopic solid materials found in plaques are not exclusively cholesterol. We observed microstructures that, whereas similar in morphology, vary in composition (mainly of pure cholesterol monohydrate and aliphatic lipids that were devoid of cholesterol). Rather than identifying crystalline material through their reflective properties, the hyperspectral CARS method assigns a chemical signature to each microstructure to avoid an erroneous identification of crystalline materials. This unique signature allows for the detailed detection of lipid composition at the most basic molecular level. Fig. 2 illustrates this point. The green and red pixels associated with the macrophages have distinct spectra, with the green spectrum exhibiting a typical neutral lipid profile and the red spectrum identifying pure cholesterol monohydrate. This discrepancy indicates the presence of ChC material within the macrophage cells, an observation not made in previous studies (30). Hence, the generation of a chemical map with spectral information contained in every single pixel allows for the visualization of cellular processes that were previously inaccessible. Furthermore, hyperspectral CARS imaging enables the identification of ChCs in nonsegmented, label-free arterial tissues with preserved three-dimensional morphology. In principle, this method can be extended to in vivo applications.

### Detection of cholesterol crystals in the mouse models

Apolipoproteins, which bind to cholesterol and other fatty acids in the plasma, are responsible for transporting and assisting the clearance of lipoproteins, such as LDL, from the plasma via the LDLR pathway in the liver. ApoE

and LDLR are not the only ligand-receptor pair; however, they constitute the majority of receptor-mediated uptake functions. Hence, deleting ApoE or LDLR in mice, in tandem with feeding a high-cholesterol diet, causes severe hypercholesterolemia and atherosclerosis (37–41). In our study, both LDLR<sup>-/-</sup> and ApoE<sup>-/-</sup> mice were fed the same high-cholesterol diet, yet large clusters of ChC were mainly observed in the ApoE<sup>-/-</sup> mouse. The distribution of ChCs in the ApoE<sup>-/-</sup> mouse extends from the region spanning the ascending aorta to the abdominal aorta, although it is predominant in the ascending aorta (data not shown). Whereas our observation of ChCs in lesions of ApoE<sup>-/-</sup> mice on a high-cholesterol diet is in agreement with previous studies (8, 9), the difference in ChC abundance and distribution in similar regions of the LDLR<sup>-/-</sup> aorta has not yet been reported, although studies have indicated ChC formation in the region of the aortic sinus (tip of the aorta) (49, 50) and the skin (51). Interestingly, in our samples, most of the ChCs observed in the aorta of the LDLR<sup>-/-</sup> model mainly exist as smaller needles, perhaps reflecting the less severe atherosclerotic state of the LDLR<sup>-/-</sup> model. This hypothesis, however, requires further investigation.

The lowered abundance of ChCs in the aortas of our LDLR<sup>-/-</sup> mice suggests a possible correlation between the absence of the ApoE lipoprotein and the formation of lipid crystals. The presence of ChC in ApoE<sup>-/-</sup>, LDLR<sup>-/-</sup> double-knockout mice supports this hypothesis (52). Furthermore, an active role for ApoE in ChC formation is supported by the observation of a significant decrease in ChC upon addition of ApoE to the culture media of J774 macrophage cells (3). Other studies have indicated an alternate pathway for LDL clearance via the LDLR-related receptor (LRP) (53, 54) and have highlighted the importance of ApoE in the formation of HDL, a marker that is inversely correlated with the progression of disease (55, 56). It has been shown that the addition of ApoE to LDLR<sup>-/-</sup>, ApoB100/100 mice does not necessarily correspond to lower cholesterol levels, but it does reduce atherosclerosis (57). Hence, it is possible that the ApoE lipoprotein may play a role in the complementary biochemical processes responsible for the inhibition of cholesterol crystals. In this regard, hyperspectral CARS imaging studies in double-knockout (ApoE<sup>-/-</sup>, LDLR<sup>-/-</sup>) mouse models and ApoE<sup>-/-</sup> or LDLR<sup>-/-</sup> models with varying diets could further help elucidate the role of ApoE lipoprotein in ChC formation. In addition, by monitoring the early stages of ChC formation along with the activation of inflammatory pathways, CARS hyperspectral imaging studies may shed new light on the role of cholesterol in stimulating an inflammatory response.

### CONCLUSION

In this study, we have demonstrated the ability to study the microscopic distribution of various lipophilic compounds within plaque lesions of atherosclerotic tissue. We implemented hyperspectral CARS imaging in combination with multivariate analysis to discriminate various lipid-rich structures, including macrophage cells and cholesterol

crystals, in two different mouse models of atherosclerosis: the LDL receptor-deficient mouse and the ApoE-deficient mouse. We have established that hyperspectral CARS imaging is capable of chemically identifying cholesterol crystals and discriminating them from other condensed aliphatic lipid microstructures in atherosclerotic plaques. While we have found cholesterol crystal aggregation throughout the aorta of 24-week-old ApoE<sup>-/-</sup> mice, the distribution of crystals in LDLR<sup>-/-</sup> mice of similar age is less abundant, thereby suggesting a possible discrepancy in plaque lesion development between the two atherosclerotic models. These findings elucidate several key aspects of the atherosclerotic mouse and provide a foundation for future studies on the role of cholesterol crystals during atherosclerotic disease progression. **LR**

### REFERENCES

- Narula, J., and H. W. Strauss. 2005. Imaging of unstable atherosclerotic lesions. *Eur. J. Nucl. Med. Mol. Imaging*. **32**: 1–5.
- Virmani, R., A. P. Burke, A. Farb, and F. D. Kolodgie. 2006. Pathology of the vulnerable plaque. *J. Am. Coll. Cardiol.* **47**: C13–C18.
- Kellner-Weibel, G., P. G. Yancey, W. G. Jerome, T. Walser, R. P. Mason, M. C. Phillips, and G. H. Rothblat. 1999. Crystallization of free cholesterol in model macrophage foam cells. *Arterioscler. Thromb. Vasc. Biol.* **19**: 1891–1898.
- Virmani, R., F. D. Kolodgie, A. P. Burke, A. V. Finn, H. K. Gold, T. N. Tulenko, S. P. Wrenn, and J. Narula. 2005. Atherosclerotic plaque progression and vulnerability to rupture: angiogenesis as a source of intraplaque hemorrhage. *Arterioscler. Thromb. Vasc. Biol.* **25**: 2054–2061.
- Falk, E., P. K. Shah, and V. Fuster. 1995. Coronary plaque disruption. *Circulation*. **92**: 657–671.
- Virmani, R., F. D. Kolodgie, A. P. Burke, A. Farb, and S. M. Schwartz. 2000. Lessons from sudden coronary death: a comprehensive morphological classification scheme for atherosclerotic lesions. *Arterioscler. Thromb. Vasc. Biol.* **20**: 1262–1275.
- Chen, Z., M. Ichetovkin, M. Kurtz, E. Zychband, D. Kawka, J. Woods, X. He, A. S. Plump, and E. Hailman. 2010. Cholesterol in human atherosclerotic plaque is a marker for underlying disease state and plaque vulnerability. *Lipids Health Dis.* **9**: 61.
- Rajamäki, K., J. Lappalainen, K. Oorni, E. Valimäki, S. Matikainen, P. T. Kovanen, and K. K. Eklund. 2010. Cholesterol crystals activate the NLRP3 inflammasome in human macrophages: a novel link between cholesterol metabolism and inflammation. *PLoS ONE*. **5**: e11765.
- Duewell, P., H. Kono, K. J. Rayner, C. M. Sirois, G. Vladimer, F. G. Bauernfeind, G. S. Abela, L. Franchi, G. Nunez, M. Schnurr, et al. 2010. NLRP3 inflammasomes are required for atherogenesis and activated by cholesterol crystals. *Nature*. **464**: 1357–1361.
- Abela, G. S. 2010. Cholesterol crystals piercing the arterial plaque and intima trigger local and systemic inflammation. *J. Clin. Lipidol.* **4**: 156–164.
- Kolodgie, F. D., A. P. Burke, G. Nakazawa, Q. Cheng, X. Xu, and R. Virmani. 2007. Free cholesterol in atherosclerotic plaques: where does it come from? *Curr. Opin. Lipidol.* **18**: 500–507.
- Abela, G. S., and K. Aziz. 2005. Cholesterol crystals cause mechanical damage to biological membranes: a proposed mechanism of plaque rupture and erosion leading to arterial thrombosis. *Clin. Cardiol.* **28**: 413–420.
- Achenbach, S., and P. Raggi. 2010. Imaging of coronary atherosclerosis by computed tomography. *Eur. Heart J.* **31**: 1442–1448.
- Amirbekian, V., M. J. Lipinski, K. C. Briley-Saebo, S. Amirbekian, J. G. Aguinaldo, D. B. Weinreb, E. Vucic, J. C. Frias, F. Hyafil, V. Mani, et al. 2007. Detecting and assessing macrophages in vivo to evaluate atherosclerosis noninvasively using molecular MRI. *Proc. Natl. Acad. Sci. USA*. **104**: 961–966.
- Sirrol, M., V. Fuster, and Z. A. Fayad. 2006. Plaque imaging and characterization using magnetic resonance imaging: towards molecular assessment. *Curr. Mol. Med.* **6**: 541–548.
- Kaufmann, B. A., and J. R. Lindner. 2007. Molecular imaging with targeted contrast ultrasound. *Curr. Opin. Biotechnol.* **18**: 11–16.

17. Cilingiroglu, M., J. H. Oh, B. Sugunan, N. J. Kemp, J. Kim, S. Lee, H. N. Zaatari, D. Escobedo, S. Thomsen, T. E. Milner, et al. 2006. Detection of vulnerable plaque in a murine model of atherosclerosis with optical coherence tomography. *Catheter. Cardiovasc. Interv.* **67**: 915–923.
18. Tearney, G. J., I. K. Jang, and B. E. Bouma. 2006. Optical coherence tomography for imaging the vulnerable plaque. *J. Biomed. Opt.* **11**: 021002.
19. Campagnola, P. J., A. C. Millard, M. Terasaki, P. E. Hoppe, C. J. Malone, and W. A. Mohler. 2002. Three-dimensional high-resolution second-harmonic generation imaging of endogenous structural proteins in biological tissues. *Biophys. J.* **82**: 493–508.
20. Zoumi, A., A. Yeh, and B. J. Tromberg. 2002. Imaging cells and extracellular matrix in vivo by using second-harmonic generation and two-photon excited fluorescence. *Proc. Natl. Acad. Sci. USA* **99**: 11014–11019.
21. Rodriguez, L. G., S. J. Lockett, and G. R. Holtom. 2006. Coherent anti-stokes Raman scattering microscopy: a biological review. *Cytometry A* **69**: 779–791.
22. Evans, C. L., and X. S. Xie. 2008. Coherent anti-stokes Raman scattering microscopy: chemical imaging for biology and medicine. *Annu. Rev. Anal. Chem. (Palo Alto Calif.)* **1**: 883–909.
23. Evans, C. L., E. O. Potma, M. Puoris'haag, D. Cote, C. P. Lin, and X. S. Xie. 2005. Chemical imaging of tissue in vivo with video-rate coherent anti-Stokes Raman scattering microscopy. *Proc. Natl. Acad. Sci. USA* **102**: 16807–16812.
24. Wang, H. W., T. T. Le, and J. X. Cheng. 2008. Label-free imaging of arterial cells and extracellular matrix using a multimodal CARS microscope. *Opt. Commun.* **281**: 1813–1822.
25. Le, T. T., I. M. Langohr, M. J. Locker, M. Sturek, and J. X. Cheng. 2007. Label-free molecular imaging of atherosclerotic lesions using multimodal nonlinear optical microscopy. *J. Biomed. Opt.* **12**: 054007.
26. Wang, H. W., I. M. Langohr, M. Sturek, and J. X. Cheng. 2009. Imaging and quantitative analysis of atherosclerotic lesions by CARS-based multimodal nonlinear optical microscopy. *Arterioscler. Thromb. Vasc. Biol.* **29**: 1342–1348.
27. Mostaço-Guidolin, L. B., M. G. Sowa, A. Ridsdale, A. F. Pegoraro, M. S. Smith, M. D. Hewko, E. K. Kohlenberg, B. Schattka, M. Shiomi, A. Stolow, et al. 2010. Differentiating atherosclerotic plaque burden in arterial tissues using femtosecond CARS-based multimodal nonlinear optical imaging. *Biomed. Opt. Express* **1**: 59–73.
28. Lim, R. S., A. Kratzer, N. P. Barry, S. Miyazaki-Anzai, M. Miyazaki, W. W. Mantulin, M. Levi, E. O. Potma, and B. J. Tromberg. 2010. Multimodal CARS microscopy determination of the impact of diet on macrophage infiltration and lipid accumulation on plaque formation in ApoE-deficient mice. *J. Lipid Res.* **51**: 1729–1737.
29. Buschman, H. P., G. Deinum, J. T. Motz, M. Fitzmaurice, J. R. Kramer, A. van der Laarse, A. V. Brusckhe, and M. S. Feld. 2001. Raman spectroscopy of human coronary atherosclerosis: biochemical assessment of cellular and extracellular morphologic structures in situ. *Cardiovasc. Pathol.* **10**: 69–82.
30. Kim, S. H., E. S. Lee, J. Y. Lee, B. S. Lee, J. E. Park, and D. W. Moon. 2010. Multiplex coherent anti-stokes Raman spectroscopy images intact atheromatous lesions and concomitantly identifies distinct chemical profiles of atherosclerotic lipids. *Circ. Res.* **106**: 1332–1341.
31. Freudiger, C. W., W. Min, G. R. Holtom, B. Xu, M. Dantus, and X. S. Xie. 2011. Highly specific label-free molecular imaging with spectrally tailored excitation-stimulated Raman scattering (STERS) microscopy. *Nat. Photonics* **5**: 103–109.
32. Lin, C. Y., J. L. Suhaim, C. L. Nien, M. D. Miljkovic, M. Diem, J. V. Jester, and E. O. Potma. 2011. Picosecond spectral coherent anti-Stokes Raman scattering imaging with principal component analysis of meibomian glands. *J. Biomed. Opt.* **16**: 021104.
33. Adams, M. J. 2004. *Chemometrics in Analytical Spectroscopy*. 2nd edition. Royal Society of Chemistry, Cambridge.
34. van der Maaten, L. J. P., E. O. Postma, and H. J. van den Herik. 2007. Dimensionality reduction: a comparative review. *Review Literature and Arts of the Americas* **10**: 1–35.
35. Chowdary, P. D., W. A. Benalcazar, Z. Jiang, D. M. Marks, S. A. Boppart, and M. Gruebele. 2010. High speed nonlinear interferometric vibrational analysis of lipids by spectral decomposition. *Anal. Chem.* **82**: 3812–3818.
36. Pohling, C., T. Buckup, and M. Motzkus. 2011. Hyperspectral data processing for chemoselective multiplex coherent anti-Stokes Raman scattering microscopy of unknown samples. *J. Biomed. Opt.* **16**: 021105.
37. Isobe, S., S. Tsimikas, J. Zhou, S. Fujimoto, M. Sarai, M. J. Branks, A. Fujimoto, L. Hofstra, C. P. Reutelingsperger, T. Murohara, et al. 2006. Noninvasive imaging of atherosclerotic lesions in apolipoprotein E-deficient and low-density-lipoprotein receptor-deficient mice with annexin A5. *J. Nucl. Med.* **47**: 1497–1505.
38. Ohshima, S., A. Petrov, S. Fujimoto, J. Zhou, M. Azure, D. S. Edwards, T. Murohara, N. Narula, S. Tsimikas, and J. Narula. 2009. Molecular imaging of matrix metalloproteinase expression in atherosclerotic plaques of mice deficient in apolipoprotein e or low-density-lipoprotein receptor. *J. Nucl. Med.* **50**: 612–617.
39. Buzello, M., J. Tornig, J. Faulhaber, H. Ehmke, E. Ritz, and K. Amann. 2003. The apolipoprotein e knockout mouse: a model documenting accelerated atherogenesis in uremia. *J. Am. Soc. Nephrol.* **14**: 311–316.
40. Hu, W., P. Polinsky, E. Sadoun, M. E. Rosenfeld, and S. M. Schwartz. 2005. Atherosclerotic lesions in the common coronary arteries of ApoE knockout mice. *Cardiovasc. Pathol.* **14**: 120–125.
41. Rattazzi, M., B. J. Bennett, F. Bea, E. A. Kirk, J. L. Ricks, M. Speer, S. M. Schwartz, C. M. Giachelli, and M. E. Rosenfeld. 2005. Calcification of advanced atherosclerotic lesions in the innominate arteries of ApoE-deficient mice: potential role of chondrocyte-like cells. *Arterioscler. Thromb. Vasc. Biol.* **25**: 1420–1425.
42. Miyazaki-Anzai, S., M. Levi, A. Kratzer, T. C. Ting, L. B. Lewis, and M. Miyazaki. 2010. Farnesoid X receptor activation prevents the development of vascular calcification in ApoE<sup>-/-</sup> mice with chronic kidney disease. *Circ. Res.* **106**: 1807–1817.
43. Pliss, A., A. N. Kuzmin, A. V. Kachynski, and P. N. Prasad. 2010. Biophotonic probing of macromolecular transformations during apoptosis. *Proc. Natl. Acad. Sci. USA* **107**: 12771–12776.
44. Faiman, R. 1977. Raman spectroscopic studies of different forms of cholesterol and its derivatives in the crystalline state. *Chem. Phys. Lipids* **18**: 84–104.
45. Brustlein, S., P. Ferrand, N. Walther, S. Brasselet, C. Billaudeau, D. Marguet, and H. Rigneault. 2011. Optical parametric oscillator-based light source for coherent Raman scattering microscopy: practical overview. *J. Biomed. Opt.* **16**: 021106.
46. Miljkovi, M., T. Chernenko, M. J. Romeo, B. Bird, C. Matthäus, and M. Diem. 2010. Label-free imaging of human cells: algorithms for image reconstruction of Raman hyperspectral datasets. *Analyst* **135**: 2002–2013.
47. Ringnér, M. 2008. What is principal component analysis? *Nat. Biotechnol.* **26**: 303–304.
48. Small, D. M., and G. G. Shipley. 1974. Physical-chemical basis of lipid deposition in atherosclerosis. *Science* **185**: 222–229.
49. Svenson, K. L., N. Ahituv, R. S. Durgin, H. Savage, P. A. Magnani, O. Foreman, B. Paigen, and L. L. Peters. 2008. A new mouse mutant for the LDL receptor identified using ENU mutagenesis. *J. Lipid Res.* **49**: 2452–2462.
50. Zhao, B., J. Song, W. N. Chow, R. W. St Clair, L. L. Rudel, and S. Ghosh. 2007. Macrophage-specific transgenic expression of cholesterol ester hydrolase significantly reduces atherosclerosis and lesion necrosis in Ldlr mice. *J. Clin. Invest.* **117**: 2983–2992.
51. Fazio, S., A. S. Major, L. L. Swift, L. A. Gleaves, M. Accad, M. F. Linton, and R. V. Farese, Jr. 2001. Increased atherosclerosis in LDL receptor-null mice lacking ACAT1 in macrophages. *J. Clin. Invest.* **107**: 163–171.
52. Jackson, C., U. Benbow, A. Bond, D. Galley, and C. Schwartz. 2010. Animal models of atherosclerosis. In *Advances in Vascular Medicine*. D. Abraham, H. Clive, M. Dashwood, et al., editors. Springer, London. 77–91.
53. Mortimer, B. C., D. J. Beveridge, I. J. Martins, and T. G. Redgrave. 1995. Intracellular localization and metabolism of chylomicron remnants in the livers of low density lipoprotein receptor-deficient mice and apoE-deficient mice. Evidence for slow metabolism via an alternative apoE-dependent pathway. *J. Biol. Chem.* **270**: 28767–28776.
54. Yu, K. C., W. Chen, and A. D. Cooper. 2001. LDL receptor-related protein mediates cell-surface clustering and hepatic sequestration of chylomicron remnants in LDLR-deficient mice. *J. Clin. Invest.* **107**: 1387–1394.
55. Tulenko, T. N., and A. E. Sumner. 2002. The physiology of lipoproteins. *J. Nucl. Cardiol.* **9**: 638–649.
56. Ishibashi, S., J. Herz, N. Maeda, J. L. Goldstein, and M. S. Brown. 1994. The two-receptor model of lipoprotein clearance: tests of the hypothesis in “knockout” mice lacking the low density lipoprotein receptor, apolipoprotein E, or both proteins. *Proc. Natl. Acad. Sci. USA* **91**: 4431–4435.
57. Thorngate, F. E., L. L. Rudel, R. L. Walzem, and D. L. Williams. 2000. Low levels of extrahepatic nonmacrophage ApoE inhibit atherosclerosis without correcting hypercholesterolemia in ApoE-deficient mice. *Arterioscler. Thromb. Vasc. Biol.* **20**: 1939–1945.